

One-Dimensional Moiré Crystals

Mikito Koshino,^{1,*} Pilkyung Moon,^{2,†} and Young-Woo Son^{3,‡}

¹*Department of Physics, Tohoku University, Sendai, 980-8578, Japan*

²*New York University Shanghai, Pudong, Shanghai 200120, China*

³*Korea Institute for Advanced Study, Seoul 130-722, Korea*

Cylindrical multishell structure is one of prevalent atomic arrangements in nanowires. Being multishell, the well-defined atomic periodicity is hardly realizable in it because the periodic units of individual shells therein cannot match well except very few cases, posing a challenge to understand its physical properties. Here we show that moiré patterns generated by superimposing atomic lattices of individual shells are decisive in determining its electronic structures. Double-walled carbon nanotubes, as an example, are shown to have spectacular variations in their electronic properties from metallic to semiconducting and further to insulating states depending on their moiré patterns even when they have only semiconducting nanotubes with almost similar energy gaps and diameters. Thus, aperiodic multishell nanowires can be classified into new one-dimensional moiré crystals with distinct electronic structures.

I. INTRODUCTION

When repetitive structures are overlaid against each other, a new superimposed moiré pattern emerges as can be observed in various macroscopic phenomena [1]. Recent progress in stacking two-dimensional crystals [2] enables the patterns occur at the atomic scale, showing their distinct quantum effects [3–6]. Even in one-dimension, this atomic pattern realizes naturally in the multishell organic and inorganic tubular shaped nanowires [7–9]. Among them, the double-walled carbon nanotubes (DWNTs) formed by two concentric single-walled carbon nanotubes (SWNTs) are the simplest multi-shell nanotube structures [10]. The electronic structure of SWNT, a basic building block of DWNTs, depends on its way of rolling a single layer graphene along a specific chiral vector into a seamless cylindrical shape. The chiral vector, $\mathbf{C} = n\mathbf{a}_1 + m\mathbf{a}_2$, or a set of integers (n, m) uniquely determines electronic structures of SWNTs where \mathbf{a}_1 and \mathbf{a}_2 are the primitive vectors of hexagonal lattice of graphene (Fig. 1(d)). They are metallic if $|n - m|$ is a multiple of three and otherwise semiconducting [10–12]. This simple rule can be obtained by reducing or quantizing one dimension of the two dimensional massless Dirac energy bands of graphene.

In spite of such a clear rule, its extension to double-walled structures is far from trivial [11–13]. Ever since its discovery [7], direct *ab initio* or empirical calculations have been performed to obtain the energy bands of DWNTs only if two single-walled nanotubes have a common periodicity along its axis [10–16]. Very few of DWNTs, however, have the commensurate condition and most of them do not have the well-defined periodicity, posing a significant challenge to understand their electronic properties [17]. This situation also holds for other

inorganic one-dimensional multishell tubular structures with several different atomic elements [9].

On the other hand, there has been a rapid progress in stacking various two-dimensional crystals and in understanding their electronic properties [2]. The most notable example among them is twisted bilayer graphene (TBLG) where a single layer graphene is overlaid on top of the other with a rotational stacking fault [18–22]. These bilayer structures exhibit moiré patterns of which periodicity is quite larger than that of the unit cell of graphene. When one layer rotates with respect to the other from zero to 60 degrees continuously, two hexagonal lattices can have a common exact supercell only for a few discrete rotation angles while they cannot have the well-defined periodic unit for infinite possible other choices of angles [21, 23–25].

Formation of moiré pattern in TBLGs, however, do not require an exact matching of atomic positions between the two layers for the common supercell. Instead, its periodicity continuously changes as the angle varies [21, 23–25]. Recent theoretical [25] and experiment [26] studies demonstrate that the electronic structure of TBLG is dictated not by the exactly matched atomic supercell but by the periodicity of moiré superlattice. Therefore, successful descriptions of the electronic structures of TBLGs without commensurability validate the effective theory [23–25, 27] based on the Bloch wave expansion with respect to the moiré lattice in momentum space. This motivates us to explore a possible dimensional reduction from modifying TBLGs with moiré patterns to one-dimensional structures which can map onto DWNTs exactly. Using the effective theory and atomic structure mapping, we uncover that the moiré pattern plays a decisive role in determining electronic structures of DWNTs without any commensurability and that the resulting properties are far beyond a simple sum of electronic bands of two constituent nanotubes.

* koshino@cmpt.phys.tohoku.ac.jp

† pilkyung.moon@nyu.edu

‡ hand@kias.re.kr

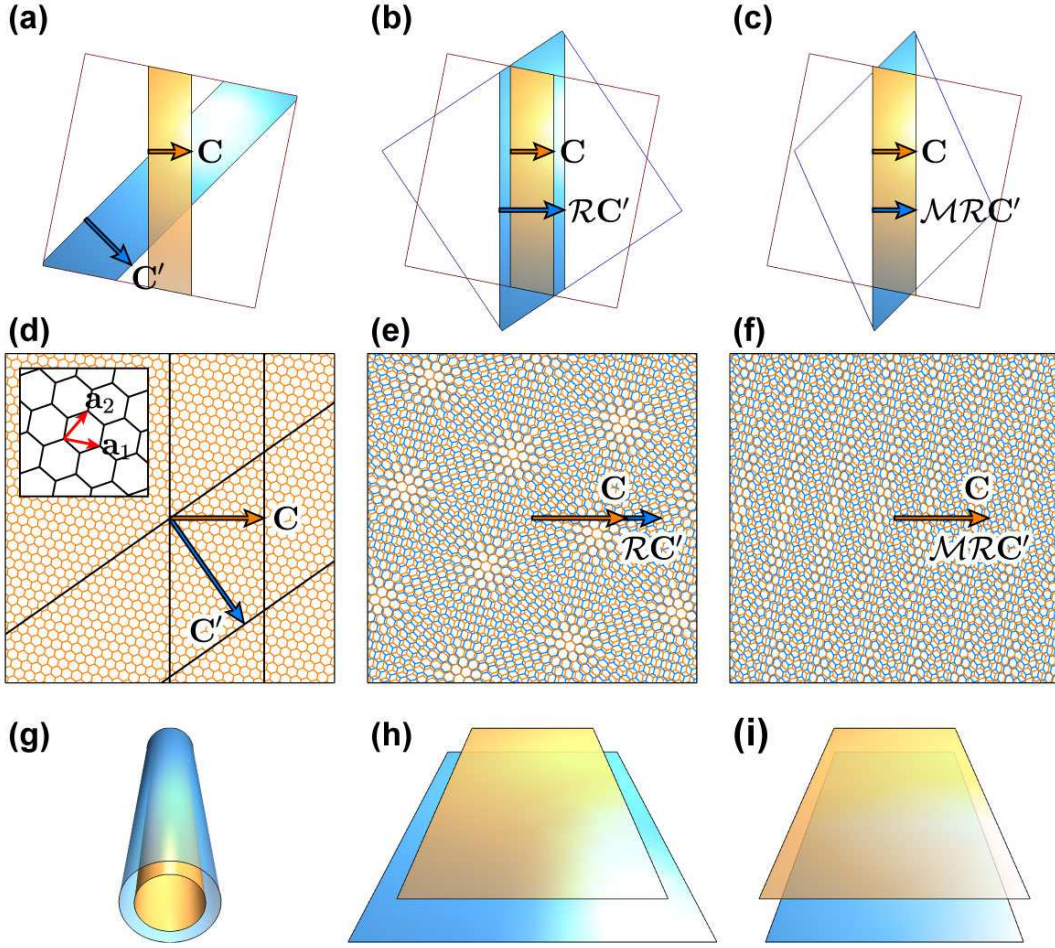


FIG. 1. Step by step operations for atomic structure mapping from graphene bilayer structure to DWNT. (a) Two parallelograms on upper and lower layers are drawn for unfolded single-walled carbon nanotubes (SWNTs) with different chiral vectors \mathbf{C} and \mathbf{C}' respectively. (b) Rotation (\mathcal{R}) and (c) subsequent contraction (\mathcal{M}) of lower layer to align the axial direction of two tubes and then to match their widths. A specific example for operations shown in (b) and (c) are displayed in (d), (e) and (f). Here we use $\mathbf{C} = 8\mathbf{a}_1 + 2\mathbf{a}_2$ and $\mathbf{C}' = 14\mathbf{a}_1 - 10\mathbf{a}_2$ for illustration where the common in-plane primitive vectors $\mathbf{a}_1 = a(1, 0)$ and $\mathbf{a}_2 = a(1/2, \sqrt{3}/2)$ with the lattice constant $a \approx 0.246$ nm are used to label the atomic positions of both layers. In (d), thin solid lines perpendicular to chiral vectors corresponds to parallelograms in (a). A usual two dimensional moiré pattern of TBLG is shown in (e) and distorted TBLG with typical moiré lattice for DWNT is in (f). Reverse mapping operations from a DWNT to double layer graphene nanoribbon are shown from (g) to (i). Unfolding (h) and then subsequent contraction of lower nanoribbon (i) map onto the modified TBLG structure ((c) and (f)) exactly.

II. MAPPING FROM BLG TO DWNT

We begin by describing atomic structure mapping procedures from bilayer graphene (BLG) to DWNT. This involves a rotation (its operator form is \mathcal{R}) and a subsequent uniaxial contraction (\mathcal{M}) of one layer with respect to the other in BLG. The upper layer is designated for the inner tube with the chiral vector of $\mathbf{C} = n_1\mathbf{a}_1 + n_2\mathbf{a}_2$ and the lower for the outer with $\mathbf{C}' = n'_1\mathbf{a}_1 + n'_2\mathbf{a}_2$ [Figs. 1(a) and 1(d)]. First, two different chiral vectors for the inner and outer SWNTs are aligned by rotating the lower layer, resulting in a usual TBLG with a moiré pattern [Figs. 1(b) and 1(e)]. After then, the lower one shrinks uniaxially along \mathbf{C} to match the two chiral vectors ex-

actly [Figs. 1(c) and 1(f)]. Resulting new primitive vectors for the lower layer become $\tilde{\mathbf{a}}_i = \mathcal{M}\mathcal{R}\mathbf{a}_i$ ($i = 1, 2$). Corresponding reciprocal lattice vectors $\tilde{\mathbf{b}}_i$ and $\tilde{\mathbf{b}}_i$ for the upper and lower layers can be defined to satisfy $\mathbf{a}_i \cdot \mathbf{b}_j = \tilde{\mathbf{a}}_i \cdot \tilde{\mathbf{b}}_j = 2\pi\delta_{ij}$ ($i, j = 1, 2$). The exactly same atomic structure can be obtained by unfolding a DWNT into a bilayer graphene nanoribbon and by subsequently shrinking the width of outer ribbon down to the inner one [Figs. 1(g) to 1(i)]. Therefore, the modified TBLG structure can match the atomic structure of DWNT with a periodic boundary condition along \mathbf{C} as shown in Fig. 1. We can alternatively map the DWNT to the modified TBLG by inversely rotating and uniaxially expanding \mathbf{C} while fixing \mathbf{C}' , but the resulting TBLG is just related to

the former by a coordinate transformation, and it does not make any actual difference in the following results.

The mismatch between lattice periods of the upper and lower layers in the modified TBLG gives rise to the moiré superlattice pattern [Figs. 2(a)-2(c)]. In this structure, the arbitrary position (\mathbf{r}) in the lower layer is displaced by $\delta(\mathbf{r}) = (\mathcal{I} - \mathcal{R}^{-1}\mathcal{M}^{-1})\mathbf{r}$ by the mapping where \mathcal{I} is an identity operator. The periodic vectors (\mathbf{L}_i^M) of emerged moiré pattern can be obtained by using a condition of $\delta(\mathbf{L}_i^M) = \mathbf{a}_i$ and are given by $\mathbf{L}_i^M = (\mathcal{I} - \mathcal{R}^{-1}\mathcal{M}^{-1})^{-1}\mathbf{a}_i$ ($i = 1, 2$). The corresponding reciprocal vectors satisfying $\mathbf{G}_i^M \cdot \mathbf{L}_j^M = 2\pi\delta_{ij}$ are given by $\mathbf{G}_i^M = (\mathcal{I} - \mathcal{M}^{-1}\mathcal{R})\mathbf{b}_i$ ($i = 1, 2$). We can immediately show that $\mathbf{G}_i^M \cdot \mathbf{C} = 2\pi(n_i - n'_i)$ ($i = 1, 2$) so that the moiré period is commensurate with the chiral vector \mathbf{C} as it should. The periodic boundary condition for DWNT forces the two-dimensional wave space be quantized into one-dimensional lines perpendicular to \mathbf{C} with intervals of $2\pi/|\mathbf{C}|$.

III. EFFECTIVE HAMILTONIAN

With the given conditions on the momentum spaces of the modified TBLG, now we construct the effective Hamiltonian for low energy electrons. The mapped lower layer for the outer tube should have distorted hexagonal Brillouin zone (BZ) while the upper layer for the inner one has a usual BZ of graphene. Figs. 2(a)-2(c) show the actual lattice structures and BZs for each of DWNTs studied in the later sections. The low energy electrons can be described by effective Hamiltonians around the each corner of intralayer BZ: $\mathbf{K}_\xi = -\xi(2\mathbf{b}_1 + \mathbf{b}_2)/3$ for the upper layer and $\tilde{\mathbf{K}}_\xi = -\xi(2\tilde{\mathbf{b}}_1 + \tilde{\mathbf{b}}_2)/3 = \mathcal{M}^{-1}\mathcal{R}\mathbf{K}_\xi$ for the lower one where $\xi = \pm 1$ denotes time-reversal partners. Near the corners, the intralayer Hamiltonians for the upper and lower layer (layer 1 and 2 hereafter) can be written as $\mathcal{H}_1(\mathbf{k}) \simeq -\hbar v(\mathbf{k} - \mathbf{K}_\xi) \cdot (\xi\sigma_x, \sigma_y)$ and $\mathcal{H}_2(\mathbf{k}) \simeq -\hbar v[\mathcal{R}^{-1}\mathcal{M}(\mathbf{k} - \tilde{\mathbf{K}}_\xi)] \cdot (\xi\sigma_x, \sigma_y)$, respectively where $\mathbf{k} = (k_x, k_y)$ is the Bloch wave number for intralayer momentum space, σ_x and σ_y are the Pauli matrices acting on the two sublattices of upper (A_1, B_1) and lower (A_2, B_2) layer, \hbar the Planck constant, and v the electron velocity of graphene. The low energy electrons of each layer interact through interlayer coupling such that the total Hamiltonian of the modified TBLG is written in the basis of (A_1, B_1, A_2, B_2) as

$$\mathcal{H}_\xi = \begin{pmatrix} \mathcal{H}_1(\mathbf{k}) & U^\dagger \\ U & \mathcal{H}_2(\mathbf{k}) \end{pmatrix}, \quad (1)$$

where U has interlayer coupling matrix elements expressed as $\langle \mathbf{k}', X'_l | T | \mathbf{k}, X_l \rangle$ where $|\mathbf{k}, X_l\rangle$ is an intralayer Bloch wave basis, X and X' are either of A or B , l and l' are either of 1 or 2, and T is an interlayer coupling Hamiltonian. These matrix elements can be explicitly written in a quite simple form with three Fourier wave

components of 1, $e^{i\xi\mathbf{G}_1^M \cdot \mathbf{r}}$ and $e^{i\xi(\mathbf{G}_1^M + \mathbf{G}_2^M) \cdot \mathbf{r}}$ as,

$$U = \begin{pmatrix} U_{A_2A_1} & U_{A_2B_1} \\ U_{B_2A_1} & U_{B_2B_1} \end{pmatrix} = u_0(d) \left[\begin{pmatrix} 1 & 1 \\ 1 & 1 \end{pmatrix} + \begin{pmatrix} 1 & \omega^{-\xi} \\ \omega^\xi & 1 \end{pmatrix} e^{i\xi\mathbf{G}_1^M \cdot \mathbf{r}} + \begin{pmatrix} 1 & \omega^\xi \\ \omega^{-\xi} & 1 \end{pmatrix} e^{i\xi(\mathbf{G}_1^M + \mathbf{G}_2^M) \cdot \mathbf{r}} \right], \quad (2)$$

where u_0 is the coupling parameter depending on intertube distance of d , and $\omega = \exp(2\pi i/3)$ (See derivations in Appendix A). Therefore, we can infer a coupling condition such that, when the distance between the two K -points of each layer, $\Delta\mathbf{K}_\xi \equiv \tilde{\mathbf{K}}_\xi - \mathbf{K}_\xi = \xi(2\mathbf{G}_1^M + \mathbf{G}_2^M)/3$, is close to either of the three Fourier components mentioned above [i.e., 0, $\xi\mathbf{G}_1^M$ or $\xi(\mathbf{G}_1^M + \mathbf{G}_2^M)$], the effect of interlayer coupling will be significant.

We note that the effective Hamiltonian in equation (1) shares essential features with those describing other two-dimensional moiré crystals such as TBLG as well as graphene on hBN monolayer. For the former case [25], $\mathcal{M} = \mathcal{I}$ while for the latter [27], \mathcal{M} is an equibiaxial expansion operator unlike the uniaxial one in the present case. However, the DWNT is not just a rolled-up version of two-dimensional moiré crystals because it has two degrees of freedom, \mathcal{M} and \mathcal{R} , depending on the choice of the inner and outer SWNTs, while the two-dimensional crystal has only the rotation degree of freedom once the two atomic layers are given. As shown in the following, the wider parameter space in the DWNT allows a number of distinct situations, that are hardly realizable in the two-dimension.

IV. ARMCHAIR AND ZIGZAG DWNTS

By numerically solving eigenvalues of equation (1) under the quantization condition of $\mathbf{k} \cdot \mathbf{C} = 2\pi N$ (N is integer), we can obtain the energy-momentum relationship of electrons in DWNTs with and without commensurability. First, the well-known results for commensurate DWNTs are reproduced by using our method [Fig. 3]. In the case of a DWNT having (n, n) SWNT inside (m, m) one [hereafter (n, n)@(m, m) DWNT], the calculated band structures from our continuum model agree well with previous results from *ab initio* methods [12] [Fig. 3(a)]. For a ($n, 0$)@($m, 0$) DWNT, the agreement between results from both methods are also very good [Figs. 3(b) and 3(c)]. In the former case, the low energy band structures deform greatly such that the two linear crossing bands push up and downward due to intertube interactions while in the latter no significant deformation can be noted. This sharp contrast can be understood by checking the coupling condition considered before. In the former case, $\Delta\mathbf{K}_\xi$ exactly coincides with $\xi\mathbf{G}_1^M$ so that all combinations of (n, n) SWNTs are always in the strong coupling condition. In the latter case, we have $\mathbf{G}_2^M = 0$ and $\Delta\mathbf{K}_\xi = (2/3)\xi\mathbf{G}_1^M$, so that $\Delta\mathbf{K}_\xi$ does not coincide

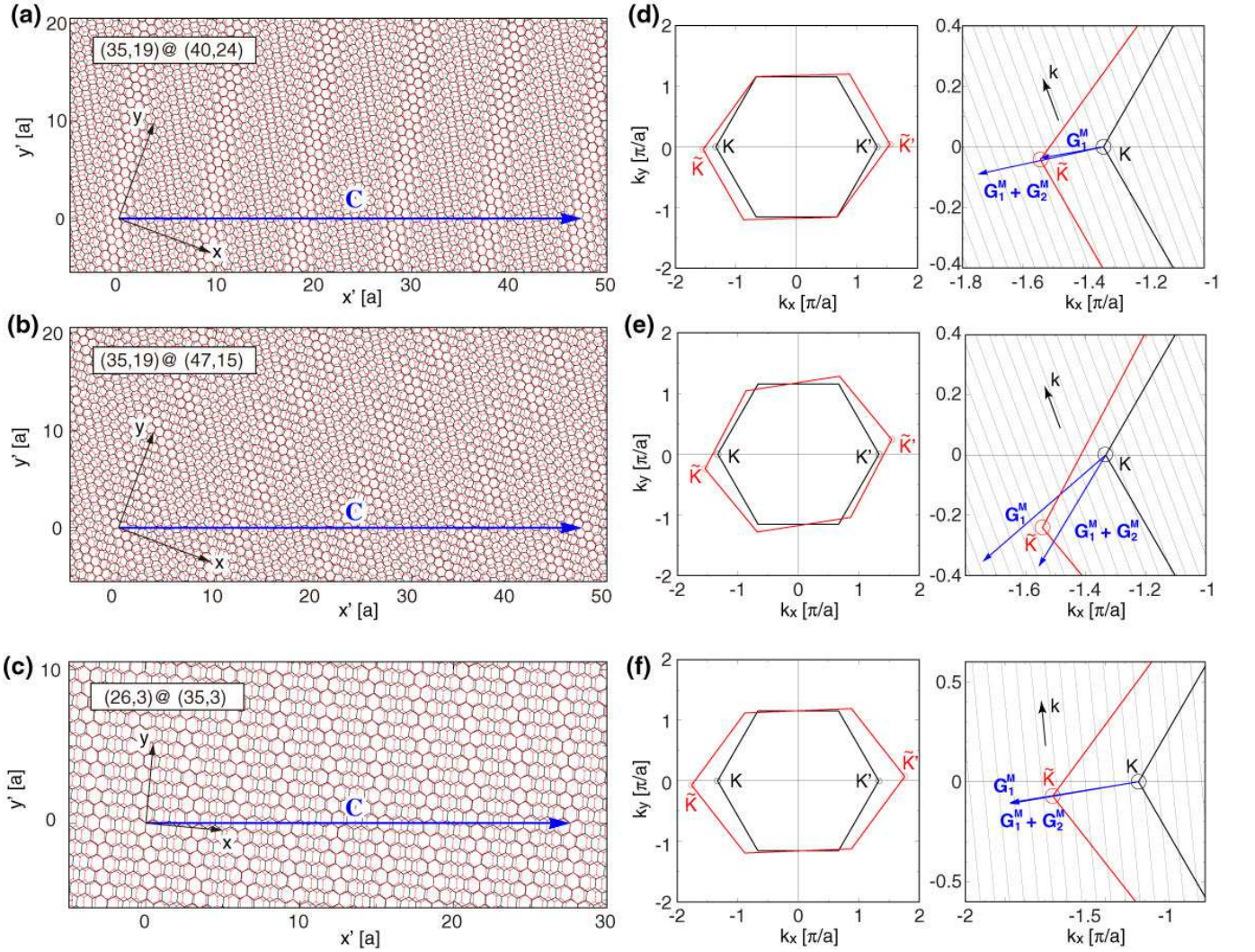


FIG. 2. After mapping operations in Fig. 1, two-dimensional atomic lattices corresponding to $(35,19)@(40,24)$, $(35,19)@(47,15)$ and $(26,3)@(35,3)$ DWNTs are drawn in (a), (b) and (c), respectively. Blue arrows are chiral vectors (\mathbf{C}) for each one. Normal (black) and distorted (red) hexagonal Brillouin zones (BZs) for three examples are presented in (d), (e) and (f) respectively. Upper (lower) Dirac points are indicated by \mathbf{K} ($\bar{\mathbf{K}}$). Enlarged BZs near around its corner are shown in the right panels. In enlarged panels, thin slant lines are one-dimensional BZs separated by $2\pi/|\mathbf{C}|$ and \mathbf{G}_i^M ($i = 1, 2$) is a reciprocal lattice vector corresponding to distorted moiré lattice.

with either of 0 , $\xi\mathbf{G}_1^M$ or $\xi(\mathbf{G}_1^M + \mathbf{G}_2^M)$, thus being in the weak coupling condition.

V. GENERAL INCOMMENSURATE DWNTS

A. Strong coupling condition

The effective continuum model and the criteria for the strong coupling work as well for incommensurate and chiral DWNTs. By measuring the distance between $\Delta\mathbf{K}_\xi$ and the three Fourier wavenumbers with varying \mathbf{C} and \mathbf{C}' , we can find all possible combinations of SWNTs to make DWNTs with strong intertube couplings. After

some algebra, the criteria for the strong coupling is reduced to the simple conditions that (i) $\mathbf{C} - \mathbf{C}'$ is parallel to the armchair direction, (ii) \mathbf{C} and \mathbf{C}' are nearly parallel (See Appendix B for the derivation). For one example, here, we choose semiconducting $(35,19)$ SWNT for inner shell and then search semiconducting outer SWNTs to show a strong or weak coupling between the two. Figure 4(a) shows the distance between $\Delta\mathbf{K}_\xi$ and $\xi\mathbf{G}_1^M$ as a function of \mathbf{C}' with \mathbf{C} fixed to $(35,19)$, where the darker color indicates smaller distance. The strong coupling region actually extends to the armchair direction as expected from the criteria discussed before. For the outer tube, we take $(40,24)$ SWNT in the strong coupling condition, and $(47,15)$ off from it, where the intertube dis-

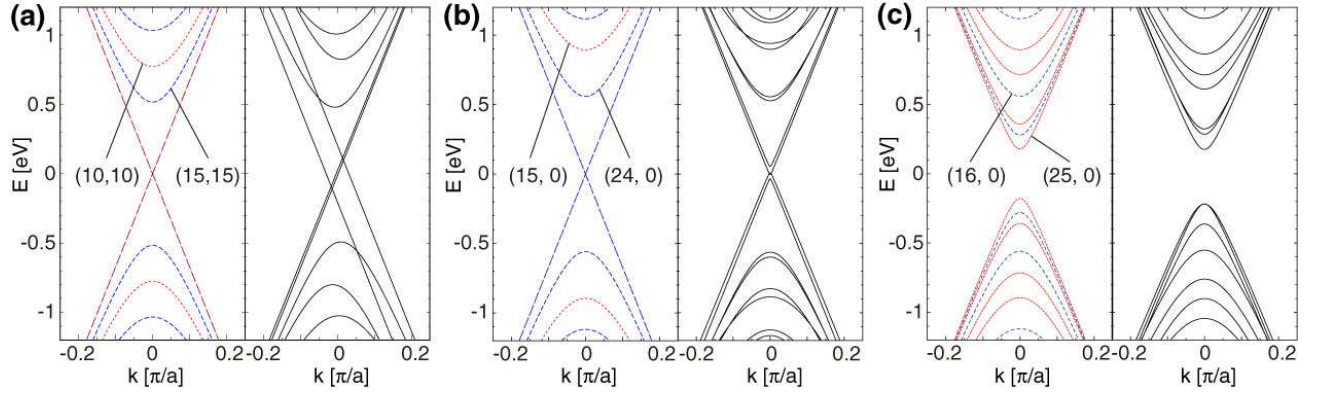


FIG. 3. Electronic energy band diagrams obtained by the atomic structure mapping and effective theory are drawn for commensurate DWNTs. (a) Energy bands of decoupled (10,10) and (15,15) SWNTs are drawn in the left panel. Red (Blue) dotted lines are for inner (outer) tubes. In the right panel, the energy bands for coupled tube, i.e., (10,10)@(15,15) DWNT is drawn. Same band diagrams for (15,0)@(24,0) and (16,0)@(25,0) DWNTs are drawn in (b) and (c), respectively. The former case is metallic and the latter semiconducting zigzag DWNT. In all band diagrams hereafter, the origin in x-axis for one-dimensional crystal momentum is taken at the K -point for metallic tubes and at the closest point to the K -point for semiconducting tubes, respectively.

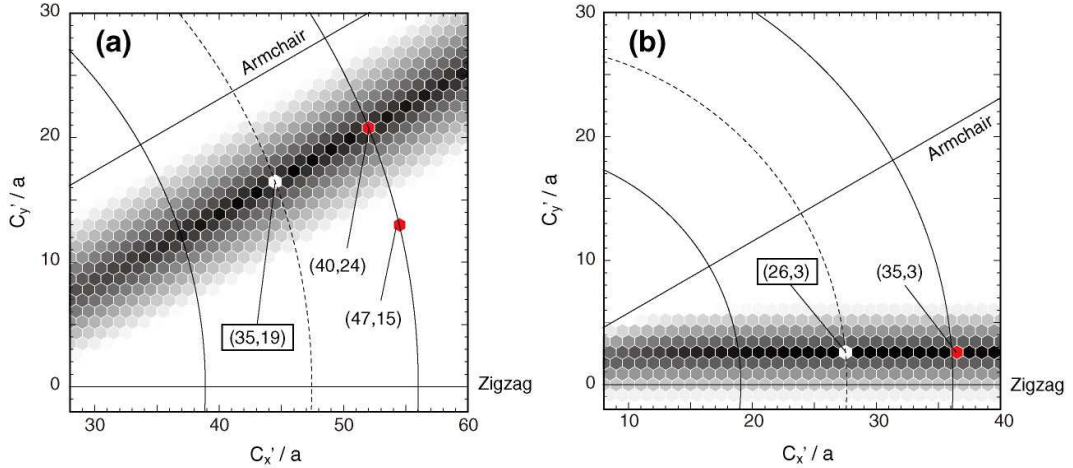


FIG. 4. (a) Two-dimensional distance map of $|\Delta\mathbf{K}_\xi - \xi\mathbf{G}_1^M|$ by varying \mathbf{C}' while \mathbf{C} is fixed to (35,19) SWNT. Here the darker colour indicates smaller distance and semicircle lines indicate same radius of SWNTs. (b) Two-dimensional map of length of \mathbf{G}_2^M as a function of \mathbf{C}' with \mathbf{C} fixed to (26,3) SWNT, where the darker colour indicates smaller length.

tance is close to the graphite's interlayer spacing in both cases. For (35,19)@(40,24) DWNT, the atomic structure of the corresponding modified TBLG and its BZ are shown in Figs. 2(a) and 2(d), respectively. We see that \mathbf{G}_1^M is indeed very close to the displacement between two K -points in Fig. 2(d). The calculated energy band structure is drawn with projected extended scheme in Fig. 5(a) (See Appendix C for the calculation method). Since the (35,19) tube has an energy band gap of 0.18 eV and (40,24) of 0.15 eV (and the curvature effect is too small to close the gap [16]), one may expect that the chiral and incommensurate DWNT composed of the two tubes will have an energy gap. However, the resulting

band structure shows the characteristic of metallic energy bands [Fig. 5(a)]. The lowest energy bands of decoupled nanotubes indeed mix together very strongly and the final low energy-momentum dispersions are quite different from the original ones. In the case of (35,19)@(47,15) DWNT [Fig. 2(b)], its energy-momentum dispersion is nothing but a simple sum of the two tubes with a slight energy shift [Fig. 5(b)] because this belongs to the weak coupling condition [Fig. 2(e)]. Corresponding density of states (DOS) for each case is displayed in Figs. 5(a) and 5(b) showing a sharp contrast between the two coupling conditions, although these two DWNTs have almost the same spectra in the absence of the intertube coupling.

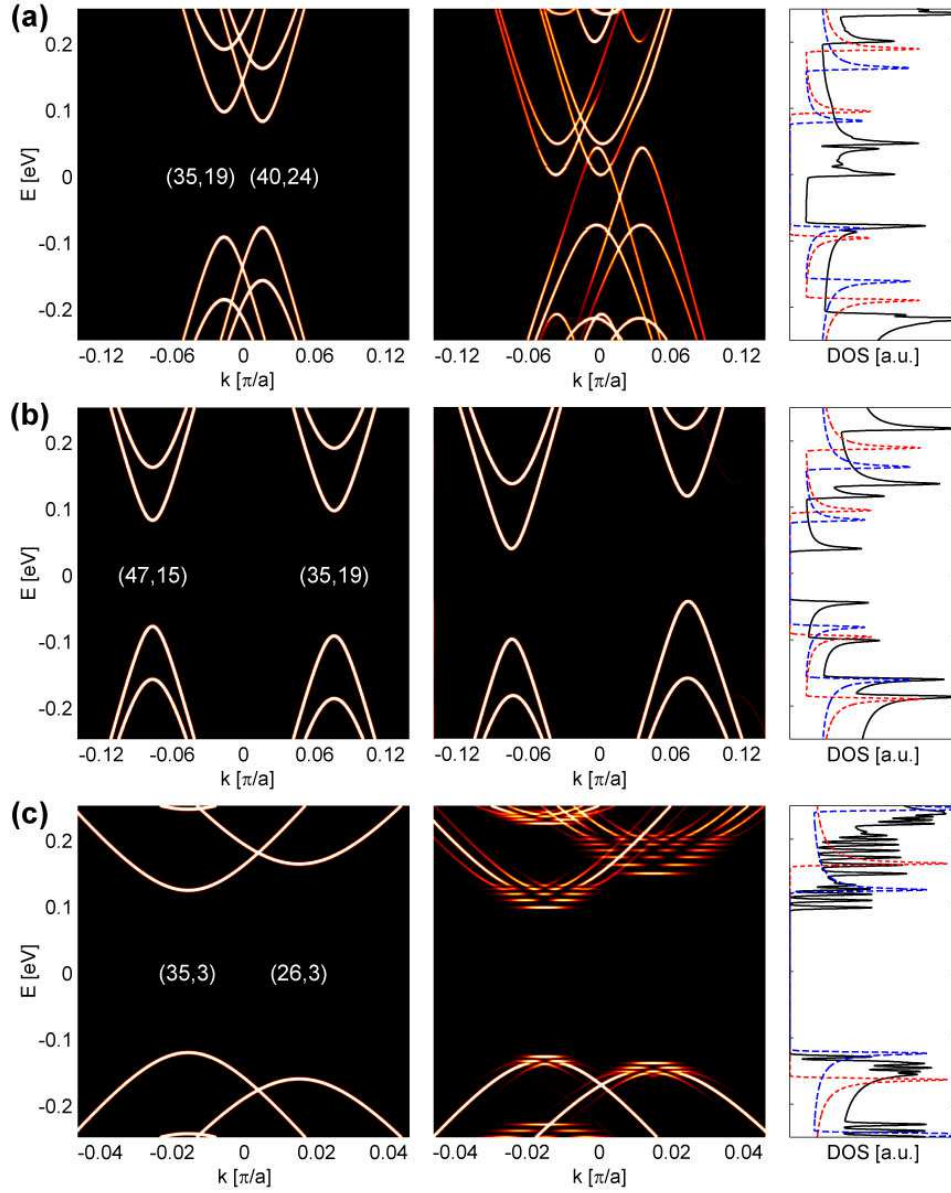


FIG. 5. Energy-momentum dispersion relation for incommensurate DWNTs are drawn with the projected extend band plot method (See Appendix C). (a) Energy bands of decoupled (35,19) and (40,24) SWNTs are drawn in the left panel. When the inter-tube coupling turns on, the dispersion of (35,19)@(40,24) DWNT is shown in the middle panel. The corresponding density of states (DOS) are drawn in the right panel. The dotted red (blue) lines are DOSs for inner (outer) nanotubes and solid black line for the coupled DWNT. Same dispersion diagrams and DOS plots for (35,19)@(47,15) and (26,3)@(35,3) DWNTs are drawn in (b) and (c), respectively. The atomic lattice structures with distorted moiré lattices and corresponding BZs for all three cases are shown in Fig. 2. For the both figures, a pair of panels in the same row belongs to specific coupling conditions: from top to bottom rows, strong, weak, and localized coupling cases.

We can further obtain an insight from analytic expression for energy gap of strongly coupled case. The low energy spectrum of strongly coupled DWNT is well approximated by the two Dirac cones separated by $\Delta\mathbf{K}_\xi$, which are directly coupled by one of three Fourier components, 0 , $\xi\mathbf{G}_1^M$ or $\xi(\mathbf{G}_1^M + \mathbf{G}_2^M)$. Suppose that the lowest energy bands of decoupled inner and outer SWNTs with respect to each band center are expressed (here $\hbar v = 1$)

as $E = \pm [m_i^2 + k^2]^{1/2}$ and $E = \pm [m_o^2 + k^2]^{1/2}$ with energy gaps of $2|m_i|$ and $2|m_o|$, respectively. When the two semiconducting SWNTs have similar diameters, we can approximate $m_i, m_o \approx m$ and then the energy bands in the presence of the intertube coupling of u_0 are approximately written as four hyperbolas (See Appendix D). If $\Delta\mathbf{K}_\xi \simeq \xi\mathbf{G}_1^M$, the four branches are given by,

$$E(k) = -u_0 \pm [(m - m_D(u_0))^2 + (k + k_D(u_0))^2]^{1/2}$$

and

$$E(k) = +u_0 \pm [(m + m_D(u_0))^2 + (k - k_D(u_0))^2]^{1/2},$$

where $m_D(u_0) = u_0\xi \cos(\phi + 60^\circ)$, $k_D(u_0) = u_0\xi \sin(\phi + 60^\circ)$, and ϕ is the angle from x -axis to \mathbf{C} . The energy gap is found to be $\Delta E = 2(|m| - u_0)$, and vanishes when $u_0 > |m|$. From these expression, we can note that the intertube interactions indeed shift and modify the bare energy bands [28] into metallic ones in the strong coupling condition.

B. Localized insulating condition

Except those two strong and weak coupling regimes, another exceptional classification is also possible for electronic structures of incommensurate DWNTs. In Figs. 2(c) and 2(f), we display a modified TBLG atomic structure and BZ for (26,3)@(35,3) DWNT. Its one dimensional energy-momentum dispersion and DOS are shown in Fig. 5(c). The two SWNTs making this DWNT are semiconducting and their chiral vectors are almost parallel with $(n,0)$ nanotubes. Unlike previous two cases, many flat bands are shown both in conduction and valence energy band as if it behaves as a series of weakly connected quantum dots and corresponding DOS also shows such a characteristic [Fig. 5(c)]. The system offers a unique situation where uniform quantum dots, containing identical energy levels, are arranged regularly at a precise period for a macroscopic length.

The flat band occurs because electronic states at contiguous k -points on the same layer are hybridized by a matrix element of U in equation (1). Then an electron on each layer feels an effective potential with very long spatial period, and the bound states appear near the bottom of the effective potential. Since the matrix U couples the different layers, we need a second order process $U^\dagger G U$ or $U G U^\dagger$ (G is Green's function of decoupled SWNTs) to connect the k -points on the same layer, and such a process has the Fourier components of $\pm \mathbf{G}_1^M$, $\pm \mathbf{G}_2^M$ and $\pm(\mathbf{G}_1^M + \mathbf{G}_2^M)$. Therefore, the flat band localization condition requires that either of \mathbf{G}_1^M , \mathbf{G}_2^M or $\mathbf{G}_1^M + \mathbf{G}_2^M$ is very small, but not exactly zero. In the case of (26,3)@(35,3) DWNT, $|\mathbf{G}_2^M|$ is merely about $0.014/a$, which corresponds to the spatial period about $450a \sim 110$ nm. Similarly to the strong coupling case, the criteria for the flat band is reduced to the simple conditions that (i) $\mathbf{C} - \mathbf{C}'$ is parallel to the zigzag direction, (ii) \mathbf{C} and \mathbf{C}' are nearly parallel (See Appendix B for the derivation). Figure 4(b) shows the length of \mathbf{G}_2^M as a function of \mathbf{C}' with the fixed \mathbf{C} of (26,3), where the flat band region actually extends to the zigzag direction.

From the last consideration, we can conclude that DWNTs with two semiconducting SWNTs can be clas-

sified into three categories, e.g., strong coupling near armchair-armchair DWNTs, localized insulating coupling near zigzag-zigzag ones and weak coupling cases otherwise. The first two cases are quite unique to the one-dimensional DWNTs and other two-dimensional heterostructures with rotational stacking faults cannot realize them with any rotation angle. This is because the strong coupling or localized insulating condition requires the matrix operation $\mathcal{M}^{-1}\mathcal{R}$ having a fixed point in two-dimensional space (see Appendix B). Such a condition, however, is never satisfied when \mathcal{M} is the identity matrix (TBLG) or equibiaxial expansion (graphene-hBN).

C. DWNTs including metallic SWNTs

Our theory is not limited to semiconducting DWNTs. When one of two or two SWNTs are metallic, three coupling conditions still hold very well. Fig. 6(a) shows the spectrum of (18,15)@(23,20) DWNT in the strong-coupling condition, where the low energy linear bands of decoupled metallic tubes are repelled away without gap opening, similar to the armchair-armchair DWNT. The localized states are also possible for DWNTs composed of metallic SWNTs, where the metallic behavior of the original SWNTs is completely lost due to the formation of the bound states at the moiré potential extrema. Fig. 6(b) and (c) show the spectra for a DWNT consisting of two metallic SWNTs [(27,3)@(36,3)], and for one consisting of a metallic SWNT and a semiconducting SWNT [(27,3)@(35,3)], respectively, both in the localized insulating condition. We observe the formation of flat bands in both cases, but in much greater energy range in (c) than in (b). The significant difference comes from the different interlayer spacing d , which gives the different interlayer coupling $u_0(d) \approx 0.07$ eV ($d \approx 0.351$ nm) in the former and 0.25 eV ($d \approx 0.312$ nm) in the latter. As the effective potential is the second order in u_0 , a change of the magnitude u_0 results in a significant difference in the energy region where the flat bands are formed. Actually the localized insulating condition strongly interferes with the condition for each SWNT to be metallic or semiconducting. We can show that a metallic-metallic DWNT in the localized insulating condition appears only when $|\mathbf{C} - \mathbf{C}'| \approx 3ma$ with integer m , and thus we have only a choice of $|\mathbf{C} - \mathbf{C}'| \approx 9a$ near the graphite interlayer spacing, which is actually the case of Fig. 6(b).

VI. CONCLUSIONS

It is evident now that combination of SWNTs with almost the same physical properties such as diameter and energy gap can end up with very different DWNTs depending on the interlayer moiré interference. Therefore, all these criteria for incommensurate and chiral DWNTs considered hitherto will dramatically influence their optical absorptions, photoluminescence, electric transport

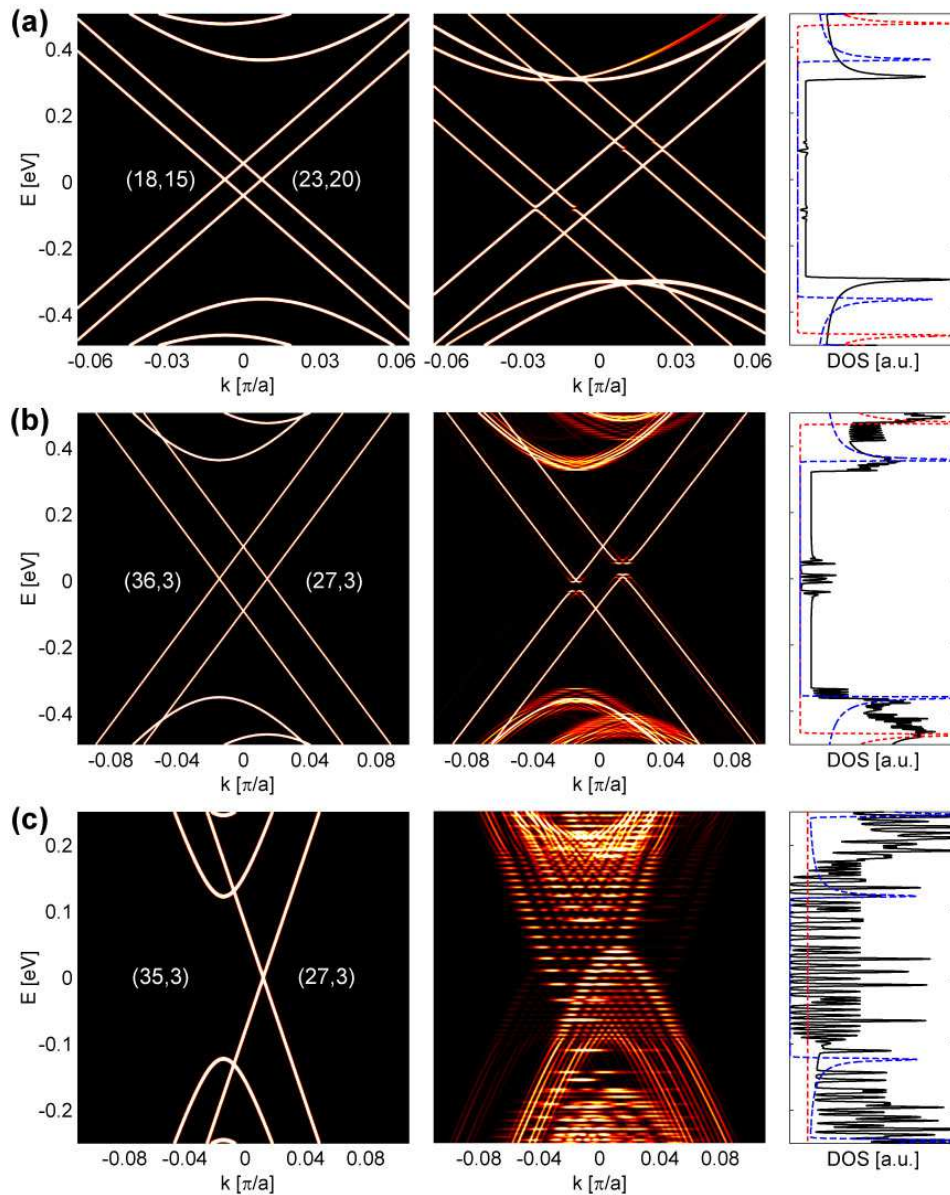


FIG. 6. (a) Energy bands of decoupled (18,15) and (23,20) SWNTs are drawn in the left panel. When the inter-tube coupling is turned on, the dispersion of (18,15)@(23,20) DWNT is shown in the middle panel. The corresponding density of states (DOS) are drawn in the right panel. The dotted red (blue) lines are DOSs for inner (outer) nanotubes and solid black line for the coupled DWNT. Same dispersion diagrams and DOS plots for (27,3)@(36,3) and (27,3)@(35,3) DWNTs are drawn in (b) and (c), respectively.

and Raman scattering that have been used for characterizing and understanding their physical properties [10–13, 29, 30]. Considering that the moiré pattern is present for almost all possible one-dimensional multishell tubular structures with several different atomic elements [9], our current theoretical framework shall not be limited to multishell carbon nanotubes also. Moreover, our study puts forth a new classification of nanotubes as the first example of one-dimensional moiré crystals and paves a firm ground to utilize superb technological merits of DWNTs [13, 29, 30].

ACKNOWLEDGMENTS

M. K. was supported by JSPS Grant-in-Aid for Scientific Research No. 24740193 and No. 25107005. P. M. was supported by New York University Shanghai Start-up Funds, and appreciate the support from East China Normal University for providing research facilities. Y.-W.S. was supported by the NRF funded by the MSIP of Korean government (CASE, 2011-0031640 and QMMRC, No. R11-2008-053-01002-0). Computations were sup-

ported by the CAC of KIAS.

Appendix A: Interlayer Hamiltonian

Here we derive the interlayer coupling matrix U in the effective Hamiltonian of DWNT, Eq. (1) in the main text. We assume that the moiré superlattice period is much larger than the lattice constant. The local lattice structure is then approximately viewed as a non-rotated bilayer graphene slided by a displacement vector $\boldsymbol{\delta}$, which slowly depends on the position \mathbf{r} as

$$\boldsymbol{\delta}(\mathbf{r}) = (\mathcal{I} - \mathcal{R}^{-1}\mathcal{M}^{-1})\mathbf{r} \quad (\text{A1})$$

as argued in the main text. Similarly to the two-dimensional moiré superlattice [25, 27], the interlayer Hamiltonian of the DWNT is obtained by replacing $\boldsymbol{\delta}$ with $\boldsymbol{\delta}(\mathbf{r})$ in the Hamiltonian of non-rotated bilayer graphene with a constant $\boldsymbol{\delta}$.

Let us consider a non-rotated bilayer graphene with a constant in-plane displacement $\boldsymbol{\delta}$ and interlayer spacing d . We define \mathbf{a}_1 and \mathbf{a}_2 as the lattice vectors of graphene, \mathbf{b}_1 and \mathbf{b}_2 as the corresponding reciprocal lattice vectors. We model the system with the tight-binding model for p_z atomic orbitals. The Hamiltonian is written as

$$H = - \sum_{\langle i,j \rangle} t(\mathbf{R}_i - \mathbf{R}_j) |\mathbf{R}_i\rangle \langle \mathbf{R}_j| + \text{H.c.}, \quad (\text{A2})$$

where \mathbf{R}_i and $|\mathbf{R}_i\rangle$ represent the lattice point and the atomic state at site i , respectively, and $t(\mathbf{R}_i - \mathbf{R}_j)$ is the transfer integral between the sites i and j . We adopt a Slater-Koster parametrization [31]

$$-t(\mathbf{R}) = V_{pp\pi} \left[1 - \left(\frac{\mathbf{R} \cdot \mathbf{e}_z}{d} \right)^2 \right] + V_{pp\sigma} \left(\frac{\mathbf{R} \cdot \mathbf{e}_z}{d} \right)^2, \\ V_{pp\pi} = V_{pp\pi}^0 e^{-(R-a_0)/r_0}, \quad V_{pp\sigma} = V_{pp\sigma}^0 e^{-(R-d_0)/r_0}, \quad (\text{A3})$$

where \mathbf{e}_z is the unit vector perpendicular to the graphene plane, $a_0 = a/\sqrt{3} \approx 0.142$ nm is the distance of neighboring A and B sites on monolayer, and $d_0 \approx 0.335$ nm is the interlayer spacing if bulk graphites. Other parameters are typically $V_{pp\pi}^0 \approx -2.7$ eV, $V_{pp\sigma}^0 \approx 0.48$ eV and $r_0 \approx 0.045$ nm. [25]

We define the Bloch wave basis of a single layer as

$$|\mathbf{k}, X_l\rangle = \frac{1}{\sqrt{N}} \sum_{\mathbf{R}_{X_l}} e^{i\mathbf{k} \cdot \mathbf{R}_{X_l}} |\mathbf{R}_{X_l}\rangle, \quad (\text{A4})$$

where $X = A, B$ is the sublattice index, $l = 1, 2$ is the layer index, and N is the number of monolayer's unit cell in the whole system. The interlayer matrix element is

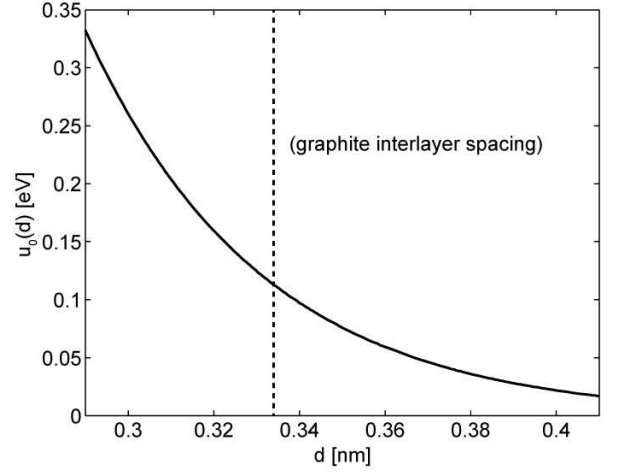


FIG. 7. Dependence of u_0 on interlayer spacing d .

then written as

$$U_{A_2A_1}(\mathbf{k}, \boldsymbol{\delta}) \equiv \langle \mathbf{k}, A_2 | H | \mathbf{k}, A_1 \rangle = u(\mathbf{k}, \boldsymbol{\delta}), \\ U_{B_2B_1}(\mathbf{k}, \boldsymbol{\delta}) \equiv \langle \mathbf{k}, B_2 | H | \mathbf{k}, B_1 \rangle = u(\mathbf{k}, \boldsymbol{\delta}), \\ U_{B_2A_1}(\mathbf{k}, \boldsymbol{\delta}) \equiv \langle \mathbf{k}, B_2 | H | \mathbf{k}, A_1 \rangle = u(\mathbf{k}, \boldsymbol{\delta} - \boldsymbol{\tau}_1), \\ U_{A_2B_1}(\mathbf{k}, \boldsymbol{\delta}) \equiv \langle \mathbf{k}, A_2 | H | \mathbf{k}, B_1 \rangle = u(\mathbf{k}, \boldsymbol{\delta} + \boldsymbol{\tau}_1), \quad (\text{A5})$$

where

$$u(\mathbf{k}, \boldsymbol{\delta}) = \sum_{n_1, n_2} -t(n_1\mathbf{a}_1 + n_2\mathbf{a}_2 + d\mathbf{e}_z + \boldsymbol{\delta}) \\ \times \exp[-i\mathbf{k} \cdot (n_1\mathbf{a}_1 + n_2\mathbf{a}_2 + \boldsymbol{\delta})]. \quad (\text{A6})$$

Here $\boldsymbol{\tau}_1 = (-\mathbf{a}_1 + 2\mathbf{a}_2)/3$ is a vector connecting the nearest A and B sublattices, and \mathbf{e}_z is the unit vector perpendicular to the graphene plane.

Since the function $u(\mathbf{k}, \boldsymbol{\delta})$ is periodic in $\boldsymbol{\delta}$ with periods \mathbf{a}_1 and \mathbf{a}_2 , it is Fourier transformed as,

$$u(\mathbf{k}, \boldsymbol{\delta}) = - \sum_{m_1, m_2} \tilde{t}(m_1\mathbf{b}_1 + m_2\mathbf{b}_2 + \mathbf{k}) \\ \times \exp[i(m_1\mathbf{b}_1 + m_2\mathbf{b}_2) \cdot \boldsymbol{\delta}], \quad (\text{A7})$$

where $\tilde{t}(\mathbf{q})$ is the in-plane Fourier transform of $t(\mathbf{R})$ defined by

$$\tilde{t}(\mathbf{q}) = \frac{1}{S} \int t(\mathbf{R} + d\mathbf{e}_z) e^{-i\mathbf{q} \cdot \mathbf{R}} d\mathbf{R}, \quad (\text{A8})$$

with $S = |\mathbf{a}_1 \times \mathbf{a}_2|$, and the integral in \mathbf{R} is taken over an infinite two-dimensional space. In the present tight-binding model, $t(\mathbf{R})$ exponentially decays in $R \gtrsim r_0$, so that the Fourier transform $\tilde{t}(\mathbf{q})$ decays in $q \gtrsim 1/r_0$. In Eq. (A7), therefore, we only need to take a few Fourier components within $|m_1\mathbf{b}_1 + m_2\mathbf{b}_2 + \mathbf{k}| \lesssim O(1/r_0)$.

In the following we only consider the electronic states near \mathbf{K}_ξ point, and then we can approximate $u(\mathbf{k}, \boldsymbol{\delta})$ with

$u(\mathbf{K}_\xi, \boldsymbol{\delta})$. Eq. (A7) then becomes

$$u(\mathbf{K}_\xi, \boldsymbol{\delta}) \approx u_0 \left[1 + e^{i\xi \mathbf{b}_1 \cdot \boldsymbol{\delta}} + e^{i\xi(\mathbf{b}_1 + \mathbf{b}_2) \cdot \boldsymbol{\delta}} \right], \quad (\text{A9})$$

with

$$u_0 = \tilde{t}(\mathbf{K}_\xi). \quad (\text{A10})$$

Note that u_0 depends on interlayer spacing d through $\tilde{t}(\mathbf{q})$ in Eq. (A8). In the present choice of the tight-binding parameters we have $u_0 = 0.11\text{eV}$ at the graphite interlayer spacing, $d = 0.334\text{ nm}$. The second largest Fourier component is $\tilde{t}(2\mathbf{K}_\xi) \approx 0.0016\text{eV}$, and is safely neglected. Unlike the graphite system, DWNTs can have wide range of d between 0.29 nm and 0.41 nm [32–35]. In this range, u_0 also varies widely from 0.33 eV to 0.017 eV , as we plot in Fig. 7. By replacing $\boldsymbol{\delta}$ with $\boldsymbol{\delta}(\mathbf{r})$ in Eq. (A1), we obtain the interlayer Hamiltonian of the DWNT, Eq. (2). Here we used the relation $\mathbf{b}_i \cdot \boldsymbol{\delta}(\mathbf{r}) = \mathbf{G}_i^M \cdot \mathbf{r}$.

Appendix B: Conditions for strong coupling case and flat band case

We derive the condition for the two chiral vectors \mathbf{C} and \mathbf{C}' to give the strong coupling case and the flat band case. The strong interlayer coupling occurs when $\Delta\mathbf{K}_\xi = \xi(2\mathbf{G}_1^M + \mathbf{G}_2^M)/3$ is close to either of 0 , $\xi\mathbf{G}_1^M$ or $\xi(\mathbf{G}_1^M + \mathbf{G}_2^M)$ (see the main text). The condition is written as

$$\begin{cases} 2\mathbf{G}_1^M + \mathbf{G}_2^M \approx 0 & \text{or} \\ \mathbf{G}_1^M - \mathbf{G}_2^M \approx 0 & \text{or} \\ \mathbf{G}_1^M + 2\mathbf{G}_2^M \approx 0. \end{cases} \quad (\text{B1})$$

Using $\mathbf{G}_i^M = (\mathcal{I} - \mathcal{M}^{-1}\mathcal{R})\mathbf{b}_i$, this is rewritten as

$$\begin{cases} (\mathcal{I} - \mathcal{M}^{-1}\mathcal{R})(2\mathbf{b}_1 + \mathbf{b}_2) \approx 0 & \text{or} \\ (\mathcal{I} - \mathcal{M}^{-1}\mathcal{R})(\mathbf{b}_1 - \mathbf{b}_2) \approx 0 & \text{or} \\ (\mathcal{I} - \mathcal{M}^{-1}\mathcal{R})(\mathbf{b}_1 + 2\mathbf{b}_2) \approx 0. \end{cases} \quad (\text{B2})$$

Since the vectors $2\mathbf{b}_1 + \mathbf{b}_2$, $\mathbf{b}_1 - \mathbf{b}_2$, and $\mathbf{b}_1 + 2\mathbf{b}_2$ are parallel to zigzag direction (i.e., $0, 2\pi/3, -2\pi/3$ from the x -axis), the condition Eq. (B2) is simplified to

$$(\mathcal{I} - \mathcal{M}^{-1}\mathcal{R})\mathbf{x} \approx 0 \quad (\text{B3})$$

for \mathbf{x} parallel to a zigzag direction.

Let us consider the amplitude of $(\mathcal{I} - \mathcal{M}^{-1}\mathcal{R})\mathbf{x}$ as a function of \mathbf{x} . We introduce a rotated coordinate system (x', y') with x' -axis set to parallel to \mathbf{C} . Then we can write

$$M = \begin{pmatrix} C/C' & 0 \\ 0 & 1 \end{pmatrix}, \quad R = \begin{pmatrix} \cos\theta & -\sin\theta \\ \sin\theta & \cos\theta \end{pmatrix}. \quad (\text{B4})$$

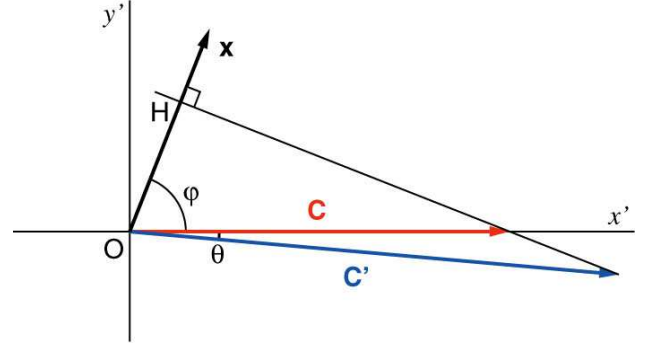


FIG. 8. Geometry to explain the strong coupling condition (see the text).

For $\mathbf{x} = (\cos\varphi, \sin\varphi)$, we have

$$\begin{aligned} |(\mathcal{I} - \mathcal{M}^{-1}\mathcal{R})\mathbf{x}|^2 &= \left(\frac{C'}{C} \cos(\varphi + \theta) - \cos\varphi \right)^2 \\ &\quad + (\sin(\varphi + \theta) - \sin\varphi)^2. \end{aligned} \quad (\text{B5})$$

The first term in the right hand side vanishes when \mathbf{x} is perpendicular to $\mathbf{C} - \mathbf{C}'$. This is geometrically explained in Fig. 8, where we actually see $\text{OH} = C' \cos(\varphi + \theta) = C \cos\varphi$ when $\mathbf{x} \perp \mathbf{C} - \mathbf{C}'$. The second term becomes small when θ is small, i.e. \mathbf{C} and \mathbf{C}' are nearly parallel. Therefore, we have strong intertube coupling when (i) $\mathbf{C} - \mathbf{C}'$ is parallel to the armchair direction (i.e., perpendicular to the zigzag direction), and (ii) \mathbf{C} and \mathbf{C}' are nearly parallel.

On the other hand, the flat band case takes place when either of \mathbf{G}_1^M , \mathbf{G}_2^M or $\mathbf{G}_1^M + \mathbf{G}_2^M$ is very close to zero, but not exactly zero. In a similar manner, the condition is rewritten as

$$\begin{cases} (\mathcal{I} - \mathcal{M}^{-1}\mathcal{R})\mathbf{b}_1 \approx 0 & \text{or} \\ (\mathcal{I} - \mathcal{M}^{-1}\mathcal{R})\mathbf{b}_2 \approx 0 & \text{or} \\ (\mathcal{I} - \mathcal{M}^{-1}\mathcal{R})(\mathbf{b}_1 + \mathbf{b}_2) \approx 0. \end{cases} \quad (\text{B6})$$

Since the vectors \mathbf{b}_1 , \mathbf{b}_2 , and $\mathbf{b}_1 + \mathbf{b}_2$ are now parallel to the armchair direction, the flat band condition is obtained by replacing "zigzag" and "armchair" in the previous argument for the strong coupling condition. Therefore, we have a flat band DWNT when (i) $\mathbf{C} - \mathbf{C}'$ is parallel to the zigzag direction, and (ii) \mathbf{C} and \mathbf{C}' are nearly parallel.

Appendix C: Calculating band structures of chiral DWNTs

We present the details of the band calculation for DWNT with the effective continuum theory. Every eigen state is labeled by the Bloch wave number \mathbf{k} defined on the cutting lines $\mathbf{k} \cdot \mathbf{C} = 2\pi N$ (N is integer) inside the two-dimensional Brillouin zone spanned by \mathbf{G}_1^M

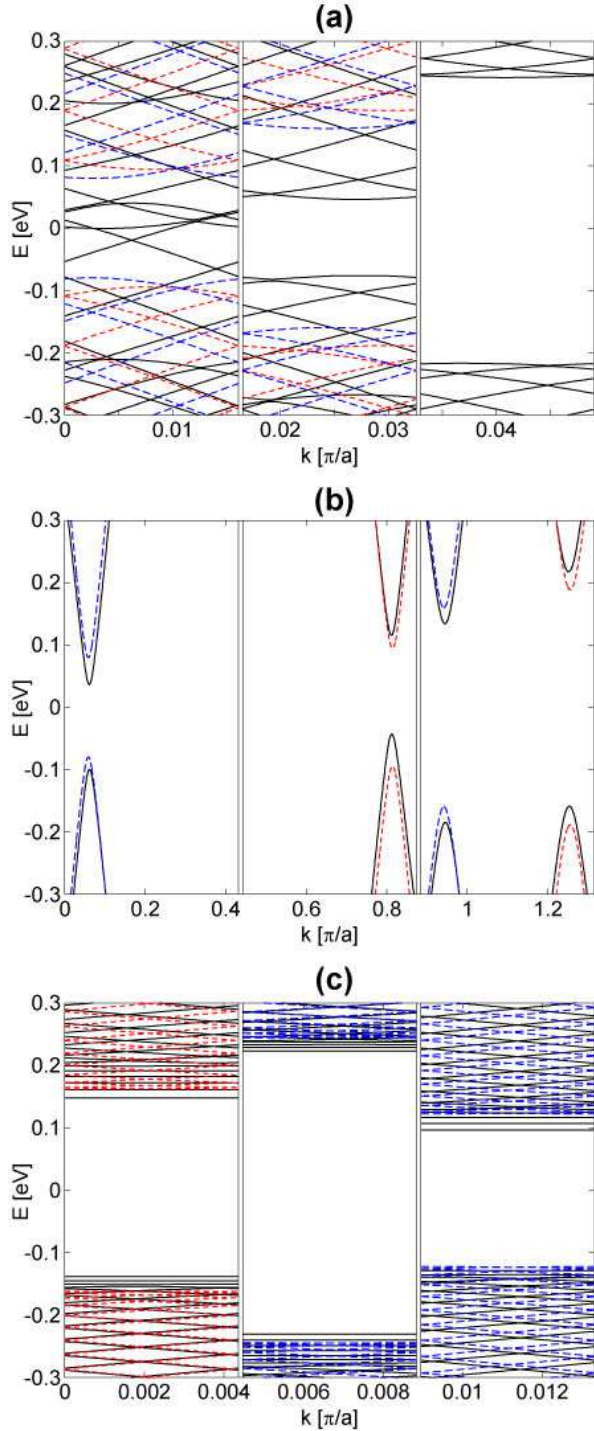


FIG. 9. Band structures near \mathbf{K}_+ valley of DWNTs with (a) (35,19)@(40,24) (strong coupling), (b) (35,19)@(47,15) (weak coupling), and (c) (26,3)@(35,3) (flat band). The solid (black) lines represent the energy bands of the DWNT in the presence interlayer coupling, while the dotted red (blue) lines are those of inner (outer) SWNTs. We do not show the subgroups which contain no energy bands in the given range.

and \mathbf{G}_2^M . Since $\mathbf{G}_i^M \cdot \mathbf{C} = 2\pi(n_i - n'_i)$, the cutting lines are categorized into n_r different subgroups where $n_r = \text{GCD}(n_1 - n'_1, n_2 - n'_2)$. To obtain the energy spectrum, we take the k -points of $\mathbf{q} = \mathbf{k} + m_1\mathbf{G}_1^M + m_2\mathbf{G}_2^M$ (m_1, m_2 : integers) in the region $|\mathbf{q} - (\mathbf{K}_\xi + \tilde{\mathbf{K}}_\xi)/2| < k_{\text{max}}$ with a sufficiently large wave-cutoff k_{max} , and numerically diagonalize the Hamiltonian within the limited wave space. Figure 9 shows the band structures of $\xi = +$ valley calculated for DWNTs studied in the main text; (a) (35,19)@(40,24), (b) (35,19)@(47,15), and (c) (26,3)@(35,3). Here the energy bands are separately plotted for each of n_r subgroups, while we omitted the subgroups which contain no energy bands in the given range. The solid curves represent the energy bands of the DWNT with the interlayer coupling, and the dotted and dashed curves are those of independent SWNTs without coupling. We actually see the band gap closing in the strong coupling case [Fig. 9(a)] and the flat low-energy bands in the flat band case [Fig. 9(c)] as argued in the main text.

In Figs. 5 and 6 in the main text, we presented the spectral function in the extended zone scheme instead of the complex band structure folded into the first Brillouin zone. This is defined as

$$A(\mathbf{k}, \varepsilon) = \sum_{\alpha} \sum_{X,l} |\langle \alpha | \mathbf{k}, X_l \rangle|^2 \delta(\varepsilon - \varepsilon_{\alpha}), \quad (\text{C1})$$

where $|\alpha\rangle$ and ε_{α} are the eigen state and the eigen energy, respectively, $X = A, B$ is the sublattice index, $l = 1, 2$ is the layer index, and $|\mathbf{k}, X_l\rangle$ is the plane wave basis defined by Eq. (A4). The spectral function is defined on the cutting lines $\mathbf{k} \cdot \mathbf{C} = 2\pi N$ on the infinite two-dimensional reciprocal space, and not limited to the reduced Brillouin zone. Figs. 5 and 6 are obtained by taking summation of the spectral functions over different cutting lines near a single K_{ξ} point, and projecting it on a single k -axis.

Appendix D: Two-mode approximation in strong interlayer coupling condition

Here we derive an approximate analytic expression of the low energy spectrum of DWNTs in the strong coupling condition. We consider the strong coupling case of $\Delta\mathbf{K}_{\xi} = \xi\mathbf{G}_1^M$, and apply the two-mode approximation for the two Dirac cones of layer 1 and 2 which are directly coupled by one of the three Fourier components, $\xi\mathbf{G}_1^M$, in the interlayer Hamiltonian. The effective Hamiltonian is written as

$$\mathcal{H}_{\text{low}} = \begin{pmatrix} \mathcal{H}_1(\mathbf{k}) & U^{\dagger} \\ U & \mathcal{H}_2(\mathbf{k}) \end{pmatrix}, \quad (\text{D1})$$

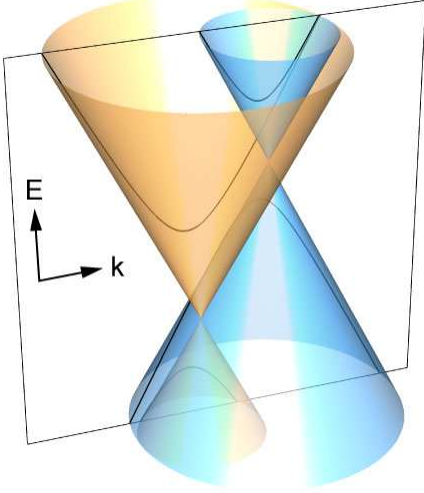


FIG. 10. Lowest energy bands of DWNT in strong coupling condition. The surface plot shows the energy dispersion of the modified TBLG, Eq. (D5). The black lines show the one-dimensional dispersion Eq. (D8) along the quantization line of semiconducting DWNT (see text).

where

$$\begin{aligned}\mathcal{H}_1(\mathbf{k}) &\simeq -\hbar v(\mathbf{k} - \mathbf{K}_\xi) \cdot (\xi\sigma_x, \sigma_y), \\ \mathcal{H}_2(\mathbf{k}) &\simeq -\hbar v[\mathcal{R}^{-1}\mathcal{M}(\mathbf{k} - \mathbf{K}_\xi - \Delta\mathbf{K}_\xi)] \cdot (\xi\sigma_x, \sigma_y), \\ U &= u_0 \begin{pmatrix} 1 & \omega^{-\xi} \\ \omega^\xi & 1 \end{pmatrix} e^{i\xi\mathbf{G}_1^M \cdot \mathbf{r}}.\end{aligned}\quad (\text{D2})$$

The two Dirac cones are separated by $\Delta\mathbf{K}_\xi$, and they are exactly merged by the Fourier component $e^{i\xi\mathbf{G}_1^M \cdot \mathbf{r}}$ since $\Delta\mathbf{K}_\xi = \xi\mathbf{G}_1^M$. By applying a unitary transformation $\mathcal{H}'_{\text{low}} = V^\dagger \mathcal{H}_{\text{low}} V$ with $V = \text{diag}(1, 1, e^{i\xi\mathbf{G}_1^M \cdot \mathbf{r}}, e^{i\xi\mathbf{G}_1^M \cdot \mathbf{r}})$, Eq. (D1) is simplified to

$$\mathcal{H}'_{\text{low}} = \begin{pmatrix} \mathcal{H}'(\mathbf{k}) & U'^\dagger \\ U' & \mathcal{H}'(\mathbf{k}) \end{pmatrix}, \quad (\text{D3})$$

with

$$\begin{aligned}\mathcal{H}'(\mathbf{k}) &= -\hbar v\mathbf{k} \cdot (\xi\sigma_x, \sigma_y), \\ U' &= u_0 \begin{pmatrix} 1 & \omega^{-\xi} \\ \omega^\xi & 1 \end{pmatrix},\end{aligned}\quad (\text{D4})$$

where the wave number \mathbf{k} is measured relative to \mathbf{K}_ξ and we use the approximation $\mathcal{R}^{-1}\mathcal{M}\mathbf{k} \approx \mathbf{k}$ assuming that $\mathcal{R}^{-1}\mathcal{M}$ is close to the identity matrix, i.e., \mathbf{C} and \mathbf{C}' sufficiently close to each other. The above equation gives the energy dispersions of two shifted Dirac cones

$$\begin{aligned}E_1^\pm(\mathbf{k}) &= -u_0 \pm \hbar v|\mathbf{k} - \mathbf{k}_0|, \\ E_2^\pm(\mathbf{k}) &= u_0 \pm \hbar v|\mathbf{k} + \mathbf{k}_0|,\end{aligned}\quad (\text{D5})$$

where $\mathbf{k} = (k_x, k_y)$ and

$$\mathbf{k}_0 \equiv \frac{u_0\xi}{\hbar v} \begin{pmatrix} \cos(-60^\circ) \\ \sin(-60^\circ) \end{pmatrix}. \quad (\text{D6})$$

The surface plot in Figure 10 shows the dispersion Eq. (D5), where we see that the two shifted Dirac cones touch on a single line $E = -\hbar v\mathbf{k} \cdot \mathbf{k}_0/|\mathbf{k}_0|$.

The lowest energy bands of DWNTs along the quantization line closest to \mathbf{K}_ξ are given as

$$\mathbf{k} = k \begin{pmatrix} -\sin\phi \\ \cos\phi \end{pmatrix} + m \begin{pmatrix} \cos\phi \\ \sin\phi \end{pmatrix}, \quad (\text{D7})$$

where ϕ is the angle from x -axis to \mathbf{C} , k is one-dimensional wave number along the tube axis, $m = 2\pi\nu\xi/(3C)$ and $\nu = 2n_1 + n_2$ (in modulo of 3) is either of 0, 1 or -1 . This gives four branches of one-dimensional energy bands

$$\begin{aligned}E_1^\pm(k) &= -u_0 \pm \hbar v\sqrt{(m - m_D(u_0))^2 + (k + k_D(u_0))^2}, \\ E_2^\pm(k) &= u_0 \pm \hbar v\sqrt{(m + m_D(u_0))^2 + (k - k_D(u_0))^2},\end{aligned}\quad (\text{D8})$$

where

$$\begin{aligned}m_D(u_0) &\equiv \frac{u_0\xi}{\hbar v} \cos(\phi + 60^\circ), \\ k_D(u_0) &\equiv \frac{u_0\xi}{\hbar v} \sin(\phi + 60^\circ).\end{aligned}\quad (\text{D9})$$

In Fig. 10, we plot the energy dispersion Eq. (D8) for the case of $\nu = 1$ with black curves, which can be recognized as the intersect between the shifted Dirac cones and k -space quantization plane.

The energy band gap of DWNT is determined by the conduction band minimum of E_1

$$E^{(c)} = -u_0 + \hbar v|m - m_D(u_0)|, \quad (\text{D10})$$

and the valence band maximum of E_2

$$E^{(v)} = u_0 - \hbar v|m + m_D(u_0)|. \quad (\text{D11})$$

The difference

$$\begin{aligned}\Delta E &= E^{(c)} - E^{(v)} \\ &= -2u_0 + \hbar v|m - m_D(u_0)| + \hbar v|m + m_D(u_0)|\end{aligned}\quad (\text{D12})$$

shows that the DWNT can have a finite gap of

$$\Delta E = 2(\hbar v|m| - u_0) \quad (\text{D13})$$

only when $\hbar v|m| \geq 2u_0$. Compared to the gap in the absence of interlayer interaction, $2\hbar v|m|$, we can see that the interlayer interaction in DWNT reduces the gap of the system by $2u_0$ in a strong coupling condition.

Figure 11(a) shows the numerically calculated band dispersions in the extend zone scheme for (35,19)@(40,24) DWNT, plotted along the quantization line closest to \mathbf{K}_ξ .

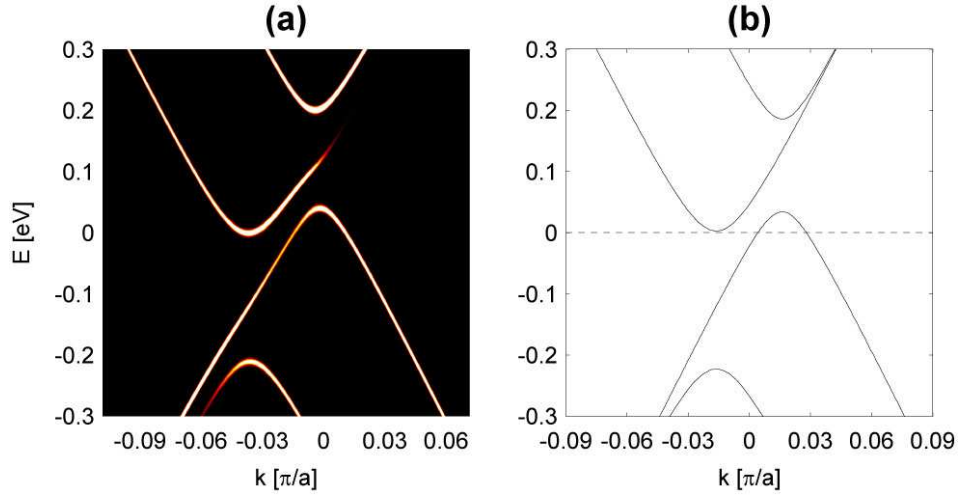


FIG. 11. (a), Numerically calculated band dispersions in the extended zone scheme for $(35,19)@(40,24)$. (b), Band dispersions of the same DWNT calculated by the analytic expression [Eq. (D8)].

We can see a good consistency with the analytic expression in Fig. 11(b), which is calculated by Eq. (D8).

Besides, since armchair-armchair DWNT is one example of the strong coupling condition, its energy dispersion

[Fig. 3(a) in the main text]

$$\begin{aligned} E_1^\pm(k) &= -u_0 \pm (\hbar vk + u_0\xi), \\ E_2^\pm(k) &= u_0 \pm (\hbar vk - u_0\xi), \end{aligned} \quad (\text{D14})$$

is also reproduced by setting $\phi = 30^\circ$ and $\nu = 0$ in Eq. (D8).

-
- [1] G. Oster and Y. Nishijima, “Moiré patterns,” *Sci. Am.* **208**, 54–63 (1963).
- [2] A. K. Geim and I. V. Grigorieva, “Van der waals heterostructures,” *Nature* **499**, 419–425 (2013).
- [3] M. Yankowitz, J. Xue, D. Cormode, J. D. Sanchez-Yamagishi, K. Watanabe, T. Taniguchi, P. Jarillo-Herrero, P. Jacquod, and B. J. LeRoy, “Emergence of superlattice dirac points in graphene on hexagonal boron nitride,” *Nat. Phys.* **8**, 382–386 (2012).
- [4] L. A. Ponomarenko, R. V. Gorbachev, Yu. G. L., D. C. Elias, R. Jalil, A. A. Patel, A. Mishchenko, A. S. Mayorov, C. R. Woods, J. R. Wallbank, M. Mucha-Kruczynski, B. A. Plot, M. Potemski, I. V. Grigorieva, K. S. Novoselov, F. Guinea, V. I. Fal’ko, and A. K. Geim, “Cloning of dirac fermions in graphene superlattices,” *Nature* **497**, 594–597 (2013).
- [5] C. R. Dean, L. Wang, P. Maher, C. Forsythe, F. Ghahari, J. and Ishigami M. Gao, Y. and Katoch, P. Moon, M. Koshino, T. Taniguchi, K. Watanabe, K. L. Shepard, J. Hone, and P. Kim, “Hofstadter’s butterfly and the fractal quantum hall effect in moire superlattices,” *Nature* **497**, 598–602 (2013).
- [6] B. Hunt, J. D. Sanchez-Yamagishi, A. F. Young, M. Yankowitz, B. J. LeRoy, K. Watanabe, T. Taniguchi, P. Moon, M. Koshino, P. Jarillo-Herrero, and R. C. Ashoori, “Massive dirac fermions and hofstadter butterfly in a van der waals heterostructure,” *Science* **340**, 1427–1430 (2013).
- [7] S. Iijima, “Helical microtubules of graphitic carbon,” *Nature* **354**, 56–58 (1991).
- [8] M. Ge and K. Sattler, “Vapor-condensation generation and stm analysis of fullerene tubes,” *Science* **260**, 515–518 (1993).
- [9] R. Tenne, “Inorganic nanotubes and fullerene-like nanoparticles,” *Nature Nanotech.* **1**, 103111 (2006).
- [10] R. Saito, G. Dresselhaus, and M. S. Dresselhaus, *Physical properties of carbon nanotubes* (Imperial College Press, 1998).
- [11] T. Ando, “Theory of electronic states and transport in carbon nanotubes,” *J. Phys. Soc. Jpn.* **74**, 777–817 (2005).
- [12] J.-C. Charlier, X. Blase, and S. Roche, “Electronic and transport properties of nanotubes,” *Rev. Mod. Phys.* **79**, 677–732 (2007).
- [13] C. Shen, A. H. Brozena, and Y. Wang, “Double-walled carbon nanotubes: Challenges and opportunities,” *Nanoscale* **3**, 503–518 (2011).
- [14] R. Saito, G. Dresselhaus, and M. S. Dresselhaus, “Electronic structure of double-layer graphene tubules,” *J. Appl. Phys.* **73**, 494–500 (1993).
- [15] J.-C. Charlier and J.-P. Michenaud, “Energetics of multi-layered carbon tubules,” *Phys. Rev. Lett.* **70**, 1858–1861 (1993).
- [16] S. Okada and A. Oshiyama, “Curvature-induced metallization of double-walled semiconducting zigzag carbon nanotubes,” *Phys. Rev. Lett.* **91**, 216801 (2003).

- [17] K.-H. Ahn, Y.-H. Kim, J. Wiersig, and K. J. Chang, “Spectral correlation in incommensurate multiwalled carbon nanotubes,” *Phys. Rev. Lett.* **90**, 026601 (2003).
- [18] J. M. B. Lopes dos Santos, N. M. R. Peres, and A. H. Castro Neto, “Graphene bilayer with a twist: Electronic structure,” *Phys. Rev. Lett.* **99**, 256802 (2007).
- [19] S. Latil, V. Meunier, and L. Henrard, “Massless fermions in multilayer graphitic systems with misoriented layers: Ab initio calculations and experimental fingerprints,” *Phys. Rev. B* **76**, 201402 (2007).
- [20] J. Hass, F. Varchon, J. E. Millán-Otoya, M. Sprinkle, N. Sharma, W. A. de Heer, C. Berger, P. N. First, L. Magaud, and E. H. Conrad, “Why multilayer graphene on 4*h*-SiC(000 $\bar{1}$) behaves like a single sheet of graphene,” *Phys. Rev. Lett.* **100**, 125504 (2008).
- [21] S. Shallcross, S. Sharma, and O. A. Pankratov, “Quantum interference at the twist boundary in graphene,” *Phys. Rev. Lett.* **101**, 056803 (2008).
- [22] M. Kindermann and P. N. First, “Local sublattice-symmetry breaking in rotationally faulted multilayer graphene,” *Phys. Rev. B* **83**, 045425 (2011).
- [23] R. Bistritzer and A. H. MacDonald, “Moiré bands in twisted double-layer graphene,” *Proceedings of the National Academy of Sciences* **108**, 12233–12237 (2011).
- [24] J. R. Wallbank, A. A. Patel, Mucha-Kruczyński M., A. K. Geim, and V. I. Fal’ko, “Generic miniband structure of graphene on a hexagonal substrate,” *Phys. Rev. B* **87**, 245408 (2013).
- [25] P. Moon and M. Koshino, “Optical absorption in twisted bilayer graphene,” *Phys. Rev. B* **87**, 205404 (2013).
- [26] R. W. Havener, Y. Liang, L. Brown, L. Yang, and J. Park, “Van hove singularities and excitonic effects in the optical conductivity of twisted bilayer graphene,” *Nano Lett.* **14**, 3353–3357 (2014).
- [27] P. Moon and M. Koshino, “Electronic properties of graphene hexagonal boron nitride moiré superlattice,” *Phys. Rev. B* **90**, 155406 (2014).
- [28] Y.-W. Son, S.-M. Choi, Y. P. Hong, S. Woo, and S.-H. Jhi, “Electronic topological transition in sliding bilayer graphene,” *Phys. Rev. B* **84**, 155410 (2011).
- [29] M. Endo, H. Muramatsu, T. Hayashi, Y. A. Kim, M. Terrones, and M. S. Dresselhaus, “‘buckypaper’ from coaxial nanotubes,” *Nature* **433**, 476 (2005).
- [30] D. Shimamoto, H. Muramatsu, T. Hayashi, Y. A. Kim, M. Endo, J. S. Park, R. Saito, M. Terrones, and M. S. Dresselhaus, “Strong and stable photoluminescence from the semiconducting inner tubes within double walled carbon nanotubes,” *Appl. Phys. Lett.* **94**, 083106 (2009).
- [31] J.C. Slater and G.F. Koster, “Simplified lcao method for the periodic potential problem,” *Phys. Rev.* **94**, 1498 (1954).
- [32] F. Villalpando-Paez, L. G. Moura, C. Fantini, H. Muramatsu, T. Hayashi, Y. A. Kim, M. Endo, M. Terrones, M. A. Pimenta, and M. S. Dresselhaus, “Tunable raman spectroscopy study of cvd and peapod-derived bundled and individual double-wall carbon nanotubes,” *Phys. Rev. B* **82**, 155416 (2010).
- [33] R. Pfeiffer, F. Simon, H. Kuzmany, V. N. Popov, V. Zolyomi, and J. Kürti, “Tube–tube interaction in double-wall carbon nanotubes,” *physica status solidi (b)* **243**, 3268–3272 (2006).
- [34] F. Villalpando-Paez, H. Son, D. Nezich, Y. P. Hsieh, J. Kong, Y. A. Kim, D. Shimamoto, H. Muramatsu, T. Hayashi, M. Endo, *et al.*, “Raman spectroscopy study of isolated double-walled carbon nanotubes with different metallic and semiconducting configurations,” *Nano Lett.* **8**, 3879–3886 (2008).
- [35] Wencai Ren, Feng Li, Jian Chen, Shuo Bai, and Hui-Ming Cheng, “Morphology, diameter distribution and raman scattering measurements of double-walled carbon nanotubes synthesized by catalytic decomposition of methane,” *Chem. Phys. Lett.* **359**, 196–202 (2002).